Stanford Exploration Project, Report 97, July 8, 1998, pages 275–294

AVO inversion in $V(x, z)$ media

Yalei Sun and Wenjie Dong[1]

keywords: *2.5-D Kirchhoff integral, AVO inversion, fluid-line section*

ABSTRACT

We implement a new Kirchhoff-typed AVO inversion scheme in $V(x, z)$ media. The WKBJ Green's function is calculated using a finite-difference scheme. We propose a pair of Kirchhoff inversion operators which have more obvious physical meaning. By analyzing the Kirchhoff inversion operator, we find out an unique relationship between the weighting function and the kinematic equation, which is very important to recover the true amplitude of the reflection coefficient. Our scheme is a two-step AVO inversion approach. Common-image gathers (CIG) are generated in the first step. These common-image gathers can be used to update the velocity model and reduce the influence of velocity error in the final AVO inversion results. AVO intercepts and slopes are estimated in the second step using a least-squares procedure. Finally, a fluid-line section is generated to highlight the existence of V_p/V_s anomaly. One dipping-layered synthetic example demonstrates the accuracy of our scheme and the influence of NMO stretch on the estimated AVO coefficients. The result from a field data example, the Mobil AVO dataset, shows a strong V_p/V_s anomaly in the middle of the section that may be a potential hydrocarbon indicator.

INTRODUCTION

Conventional AVO analysis extracts the intercept and slope from NMO-corrected CMP gathers. Since no imaging capability is incorporated, diffraction energy is not properly analyzed. Diffraction-corrupted intercept and slope sections may lead to false hydrocarbon indications. The influence of migration/inversion on AVO analysis has been addressed by several authors (Lumley et al., 1995; Mosher et al., 1996; Dong and Keys, 1997). Lumley et al. (1995) use the conventional common-offset prestack time migration to collapse the diffraction energy. Mosher et al. (1996) also use the prestack time migration technique. In order to improve the lateral resolution and spatial positioning of AVO anomalies, they choose common-angle sections instead of common-offset sections. The most important problem with the time migration schemes is that they cannot handle large lateral velocity and structure variations

[1]**email:** yalei@sep.stanford.edu,wenjie_dong@email.mobil.com

easily. The time imaging error will consequently produce mispositioning of AVO anomalies in the spatial domain. Dong and Keys (1997) propose a prestack depth inversion scheme. They assume that the earth satisfies a locally 1-D layered velocity model to make the algorithm efficient. The inversion is of Kirchhoff-typed and implemented in the common-midpoint gather. This locally 1-D assumption restricts their schemes to handle only moderate lateral velocity and structure variations. In this paper, we propose an AVO inversion scheme for 2-D media. The WKBJ Green's function is calculated by a finite-difference algorithm. A 2.5-D Kirchhoff integral is used in the inversion. Common-image gathers (CIG) are produced as a by-product, that can be used to quality-control the accuracy of velocity model. We first derive a new form of the 2.5-D Kirchhoff integral formula in $V(x,z)$ media and relate it to the WKBJ Green's function. Then we discuss the characteristics of the weighting function in the Kirchhoff integral. We show the effect of the integral aperture on the estimated amplitude of the reflection coefficient. Finally, we discuss the results of applying the new algorithm to synthetic and field data.

THEORY OF 2.5-D KIRCHHOFF INVERSION IN $V(X,Z)$ MEDIA

In the spatial and frequency domain, the 3-D acoustic wave equation can be formulated as

$$\left[\nabla^2 + \frac{\omega^2}{c^2(\mathbf{x})}\right] G(\mathbf{x}, \mathbf{x}_s, \omega) = -\delta(\mathbf{x} - \mathbf{x}_s) \tag{1}$$

where $G(\mathbf{x}, \mathbf{x}_s, \omega)$ can be approximated by the WKBJ Green's function

$$G(\mathbf{x}, \mathbf{x}_s, \omega) \sim A(\mathbf{x}, \mathbf{x}_s) e^{i\omega\tau(\mathbf{x},\mathbf{x}_s)} \tag{2}$$

where $\tau(\mathbf{x}, \mathbf{x}_s)$ is the traveltime from source $\mathbf{x}_s$ to an arbitrary point $\mathbf{x}$. Using the WKBJ Green's function, Beylkin (1985) gave an inversion formula in 3-D media

$$\alpha(\mathbf{x}) \sim \frac{c^2(\mathbf{x})}{8\pi^3} \int\int_{S_0} d^2\xi \frac{|h(\mathbf{x},\xi)|}{A(\mathbf{x},\mathbf{x}_s)A(\mathbf{x},\mathbf{x}_r)} \int d\omega F(\omega) e^{-i\omega[\tau(\mathbf{x},\mathbf{x}_s)+\tau(\mathbf{x},\mathbf{x}_r)]} D(\omega,\xi). \tag{3}$$

In the above formula, $\alpha(\mathbf{x})$ is the perturbation to the background velocity $c(\mathbf{x})$. The updated velocity model is given by

$$v^{-2}(\mathbf{x}) = c^{-2}(\mathbf{x}) \left[1 + \alpha(\mathbf{x})\right]. \tag{4}$$

S_0 is the 2-D integral surface. $h(\mathbf{x},\xi)$ is introduced by Beylkin (1985), which is associated with the ray curvature. $A(\mathbf{x},\mathbf{x}_s)$ and $A(\mathbf{x},\mathbf{x}_r)$ are the WKBJ Green's function. $F(\omega)$ is a high-pass filter determined the source. $D(\omega,\xi)$ represents the observed data at $\mathbf{x}_r$ due to the source $\mathbf{x}_s$. Bleistein et al.(1987) specialize the 3-D formula to the 2.5-D geometry using the method of stationary phase. The corresponding 2.5-D inversion formula is

$$\alpha(\mathbf{x}) \;\sim\; 2\sqrt{\frac{2}{\pi}} \int d\xi \left[1 + c^2(\mathbf{x})\mathbf{p}_s \cdot \mathbf{p}_r\right]$$

$$\sqrt{\frac{1}{\sigma_{s_0}}+\frac{1}{\sigma_{r_0}}}\left(\hat{\mathbf{n}}_s\cdot\mathbf{p}_{s_0}\frac{A_s}{A_r}\sigma_{s_0}+\hat{\mathbf{n}}_r\cdot\mathbf{p}_{r_0}\frac{A_r}{A_s}\sigma_{r_0}\right)$$
$$\int\frac{d\omega}{\sqrt{i\omega}}F(\omega)e^{-i\omega(\tau_s+\tau_r)}D(\omega,\xi) \tag{5}$$

Here, $\mathbf{p}_s$ and $\mathbf{p}_r$ are the slowness vectors at the imaging location pointing to the source and receiver respectively. σ_{s_0} and σ_{r_0} are the parameters defined by the following equations

$$\sigma_{s_0}=\int_0^{\tau_s}c(\mathbf{x})d\tau, \qquad \sigma_{r_0}=\int_0^{\tau_r}c(\mathbf{x})d\tau. \tag{6}$$

$\hat{\mathbf{n}}_s$ and $\hat{\mathbf{n}}_r$ are unit downward normals at the source and receiver points respectively. $\mathbf{p}_{s_0}$ and $\mathbf{p}_{r_0}$ are the slowness vectors at the source and receiver points respectively. This inversion formula is only valid in the high-frequency limit. Under such circumstances, it is better to process data for the upward normal derivative $\partial\alpha/\partial n$ at each discontinuity surface of $\alpha(\mathbf{x})$. $\partial\alpha/\partial n$ is a sum of weighted singular functions with peaks on the reflectors. Therefore, $\partial\alpha/\partial n$ actually provides an image of the subsurface. Using the Fourier transform, we can obtain the following 2.5-D formula for $\partial\alpha/\partial n$.

$$\begin{aligned}\frac{\partial\alpha}{\partial n}(\mathbf{x}) \quad \sim \quad & \frac{4}{\sqrt{\pi}c(\mathbf{x})}\int d\xi\left[1+c^2(\mathbf{x})\mathbf{p}_s\cdot\mathbf{p}_r\right]^{\frac{3}{2}}\\ & [A_sA_r]^{-1}\sqrt{\frac{1}{\sigma_{s_0}}+\frac{1}{\sigma_{r_0}}}\left[\hat{\mathbf{n}}_s\cdot\mathbf{p}_{s_0}A_s^2(\mathbf{x},\mathbf{x}_s)\sigma_{s_0}+\hat{\mathbf{n}}_r\cdot\mathbf{p}_{r_0}A_r^2(\mathbf{x},\mathbf{x}_r)\sigma_{r_0}\right]\\ & \int d\omega\sqrt{i\omega}F(\omega)e^{-i\omega(\tau_s+\tau_r)}D(\omega,\xi)\end{aligned} \tag{7}$$

Bleistein et al.(1987) also shows that $\partial\alpha/\partial n$ can be related to the reflection coefficient on the interface by

$$\frac{\partial\alpha}{\partial n}\sim 4\cos^2\theta R(\mathbf{x},\theta)\gamma(\mathbf{x}) \tag{8}$$

$\gamma(\mathbf{x})$ in the singular function of the model space. $R(\mathbf{x},\theta)$ is determined by the changes of velocity and density above and below the interface and the incident angle on the interface

$$R(\mathbf{x},\theta)=\frac{c_{down}(\mathbf{x})\rho_{down}\cos\theta-\rho_{up}\sqrt{c_{up}^2(\mathbf{x})-c_{down}^2(\mathbf{x})\sin^2\theta}}{c_{down}(\mathbf{x})\rho_{down}\cos\theta+\rho_{up}\sqrt{c_{up}^2(\mathbf{x})-c_{down}^2(\mathbf{x})\sin^2\theta}}. \tag{9}$$

In order to determine $R(\mathbf{x},\theta)$ from $\partial\alpha/\partial n$, we have to determine $\cos\theta$. In their paper, Bleistein et al.(1987) proposed another inversion operator $\beta(x,z)$ with a kernel slightly modified from that in $\partial\alpha/\partial n$.

$$\begin{aligned}\beta(\mathbf{x}) \quad \sim \quad & \frac{2}{\sqrt{\pi}c(\mathbf{x})}\int d\xi\left[1+c^2(\mathbf{x})\mathbf{p}_s\cdot\mathbf{p}_{\mathbf{r}}\right]^{\frac{1}{2}}\\ & [A_sA_r]^{-1}\sqrt{\frac{1}{\sigma_{s_0}}+\frac{1}{\sigma_{r_0}}}\left[\hat{\mathbf{n}}_s\cdot\mathbf{p}_{s_0}A_s^2(\mathbf{x},\mathbf{x}_s)\sigma_{s_0}+\hat{\mathbf{n}}_r\cdot\mathbf{p}_{r_0}A_r^2(\mathbf{x},\mathbf{x}_r)\sigma_{r_0}\right]\\ & \int d\omega\sqrt{i\omega}F(\omega)e^{-i\omega(\tau_s+\tau_r)}D(\omega,\xi)\end{aligned} \tag{10}$$

There is a simple relation between $\partial\alpha/\partial n$, $\beta(x,z)$, and $\cos\theta$, that is

$$\cos^2\theta = \frac{\frac{\partial\alpha}{\partial n}(peak)}{4\beta(peak)}. \tag{11}$$

With $\cos\theta$ known, we can use $\partial\alpha/\partial n$ and $\cos\theta$ to calculate the reflection coefficient $R(\mathbf{x},\theta)$. From $R(\mathbf{x},\theta)$ and $\cos\theta$, we can further estimate the AVO coefficients: intercept and slope. Instead of using $\partial\alpha/\partial n$ and $\beta(x,z)$, we propose another pair of inversion operators that can determine $\cos\theta$ in a similar, but more straightforward and physically meaningful manner. The first operator gives the reflection coefficient at the specular incident angle

$$\begin{aligned} R(\mathbf{x},\theta) \sim\ & \frac{1}{\sqrt{\pi}c(\mathbf{x})}\int d\xi \\ & [A_sA_r]^{-1}\sqrt{\frac{1}{\sigma_{s_0}}+\frac{1}{\sigma_{r_0}}}\left[\hat{\mathbf{n}}_s\cdot\mathbf{p}_{s0}A_s^2(\mathbf{x},\mathbf{x}_s)\sigma_{s_0}+\hat{\mathbf{n}}_r\cdot\mathbf{p}_{r0}A_r^2(\mathbf{x},\mathbf{x}_r)\sigma_{r_0}\right] \\ & \int d\omega\sqrt{i\omega}F(\omega)e^{-i\omega(\tau_s+\tau_r)}D(\omega,\xi) \end{aligned} \tag{12}$$

The second gives the reflection coefficient multiplied by $\cos\theta$

$$\begin{aligned} R'(\mathbf{x},\theta) \sim\ & \frac{1}{\sqrt{2\pi}c(\mathbf{x})}\int d\xi\left[1+c^2(\mathbf{x})\mathbf{p}_s\cdot\mathbf{p}_r\right]^{\frac{1}{2}} \\ & [A_sA_r]^{-1}\sqrt{\frac{1}{\sigma_{s_0}}+\frac{1}{\sigma_{r_0}}}\left[\hat{\mathbf{n}}_s\cdot\mathbf{p}_{s0}A_s^2(\mathbf{x},\mathbf{x}_s)\sigma_{s_0}+\hat{\mathbf{n}}_r\cdot\mathbf{p}_{r0}A_r^2(\mathbf{x},\mathbf{x}_r)\sigma_{r_0}\right] \\ & \int d\omega\sqrt{i\omega}F(\omega)e^{-i\omega(\tau_s+\tau_r)}D(\omega,\xi) \end{aligned} \tag{13}$$

From $R(\mathbf{x},\theta)$ and $R'(\mathbf{x},\theta)$, we can easily calculate $\cos\theta$

$$\cos\theta = \frac{R'(\mathbf{x},\theta)}{R(\mathbf{x},\theta)}. \tag{14}$$

In order to reduce the sensitivity of $\cos\theta$ to noise in the data, we use a least-squares procedures to estimate $\cos\theta$. First, we define a small window ($n_x \times n_z$). Within the window, we can get a series of equations

$$\begin{array}{rcl} R(x_1,z_1,\theta)\cos\theta & = & R'(x_1,z_1,\theta) \\ R(x_2,z_2,\theta)\cos\theta & = & R'(x_2,z_2,\theta) \\ & \cdot & \\ & \cdot & \\ & \cdot & \\ R(x_n,z_n,\theta)\cos\theta & = & R'(x_n,z_n,\theta) \end{array} \tag{15}$$

the least-squares sense estimate of $\cos\theta$ is then

$$\cos\theta = \frac{\sum_{x_i,z_i}^{n} R(x_1,z_1,\theta)R'(x_1,z_1,\theta)}{\sum_{x_i,z_i}^{n} R^2(x_1,z_1,\theta)}. \tag{16}$$

AVO THEORY IN ACOUSTIC AND ELASTIC MEDIA

Under the assumption of small incident angle, there is a well-known linearized Zoeppritz equation (Aki and Richards, 1980). Because we only consider the incident angle less than 35 degree, we have omitted the C term in the original form. For the acoustic and elastic media, the expressions for the reflection coefficients are different.

Acoustic AVO approximation

$$R \approx A + B\tan^2\theta \tag{17}$$

where

$$\begin{aligned} A &\approx \frac{1}{2}\left(\frac{\delta V}{V} + \frac{\delta\rho}{\rho}\right) \\ B &\approx \frac{1}{2}\frac{\delta V}{V} \end{aligned} \tag{18}$$

Elastic AVO approximation

$$R \approx A + B\sin^2\theta \tag{19}$$

where

$$\begin{aligned} A &\approx \frac{1}{2}\left(\frac{\delta V_p}{V_p} + \frac{\delta\rho}{\rho}\right) \\ B &\approx \frac{1}{2}\frac{\delta V_p}{V_p} - 2\left(\frac{V_s}{V_p}\right)^2\left(2\frac{\delta V_s}{V_s} + \frac{\delta\rho}{\rho}\right) \end{aligned} \tag{20}$$

Using the reflection coefficient R and specular incident angle θ, we find the solution for intercept and slope is a least-squares problem.

$$\begin{aligned} R_1 &= A + Bf(\theta_1) \\ R_2 &= A + Bf(\theta_2) \\ &\ \ \vdots \\ R_n &= A + Bf(\theta_n) \end{aligned} \tag{21}$$

The resulting estimates of A and B are given by

$$\begin{bmatrix} A \\ B \end{bmatrix} = \begin{bmatrix} N & \sum_i^N f(\theta_i) \\ \sum_i^N f(\theta_i) & \sum_i^N f^2(\theta_i) \end{bmatrix} \begin{bmatrix} \sum_i^N R_i \\ \sum_i^N R_i f(\theta_i) \end{bmatrix} \tag{22}$$

Getting AVO intercept and slope is not our final goal. The purpose of AVO analysis is to display the V_p/V_s anomaly in the subsurface. This anomaly is a very important hydrocarbon indication, especially for gas-charged reservoirs. Here we use the fluid-line technique to highlight this anomaly. Assume there is a linear relation

$$AX + B = 0 \tag{23}$$

between intercept A and slope B. We specify a window with reasonable size and use least squares algorithm to estimate the coefficient X. Similar to $\cos\theta$, we get an expression for X

$$X = \frac{\sum_{x_i,z_i}^{n} A(x_i,z_i)B(x_i,z_i)}{\sum_{x_i,z_i}^{n} A^2(x_i,z_i)}. \tag{24}$$

The $AX+B$ section is called the *fluid-line* section, which highlights the V_p/V_s anomaly.

PARAMETER ANALYSIS

The 2.5-D Kirchhoff inversion can be viewed as a weighted Kirchhoff depth migration. In other words, if there is no middle row in equation (12), the final result will be a 2-D Kirchhoff depth migration in $V(x,z)$ media. In this section, we investigate the relationship between the two key components in equation (12) in the homogeneous medium.

Weighting function

The weighting function determines the contribution of each data sample to the image. The weighting function depends on the locations of source, receiver, and diffractor.

$$w(\mathbf{x}_s,\mathbf{x}_r;\mathbf{x}) = [A_sA_r]^{-1}\sqrt{\frac{1}{\sigma_{s_0}}+\frac{1}{\sigma_{r_0}}}\left[\hat{\mathbf{n}}_s\cdot\mathbf{p}_{s_0}A_s^2(\mathbf{x},\mathbf{x}_s)\sigma_{s_0}+\hat{\mathbf{n}}_r\cdot\mathbf{p}_{r_0}A_r^2(\mathbf{x},\mathbf{x}_r)\sigma_{r_0}\right] \tag{25}$$

Double-square-root (DSR) equation

The DSR equation is the kinematic relation between source, receiver, and diffractor in the homogeneous media.

$$\begin{aligned}\tau(\mathbf{x}_s,\mathbf{x}_r;\mathbf{x}) &= \tau_s+\tau_r \\ &= \frac{1}{V}\left(\sqrt{(x_s-x)^2+(z_s-z)^2}+\sqrt{(x_r-x)^2+(z_r-z)^2}\right)\end{aligned} \tag{26}$$

It is worth investigating the relationship between these two components and other parameters, such as image depth, integral aperture, velocity, and offset, etc. In order to simplify the problem, we assume a homogeneous media and discuss the dependence of weighting function and DSR equation on other parameters, such as offset, depth, and velocity. The DSR equation is a function of imaging depth, velocity, and offset. As shown in Figure 1, with increasing imaging depth, the hyperbolic curve becomes flatter. Therefore, anti-aliasing requirements in the deep zone are not as severe as it is in the shallow zone. Similarly, high velocity corresponds to a flattened hyperbola. Large offset has a similar effect. Actually, if we view the offset response in 3-D, it is the famous "Cheops pyramid" (Claerbout, 1985). We then take the first and second derivatives of the hyperbolic curves. As show in Figure 2, with the increase of offset, the first derivative has two inflection points. Correspondingly, two peak values show up in the second derivative for non-zero offset. In a constant velocity medium, the

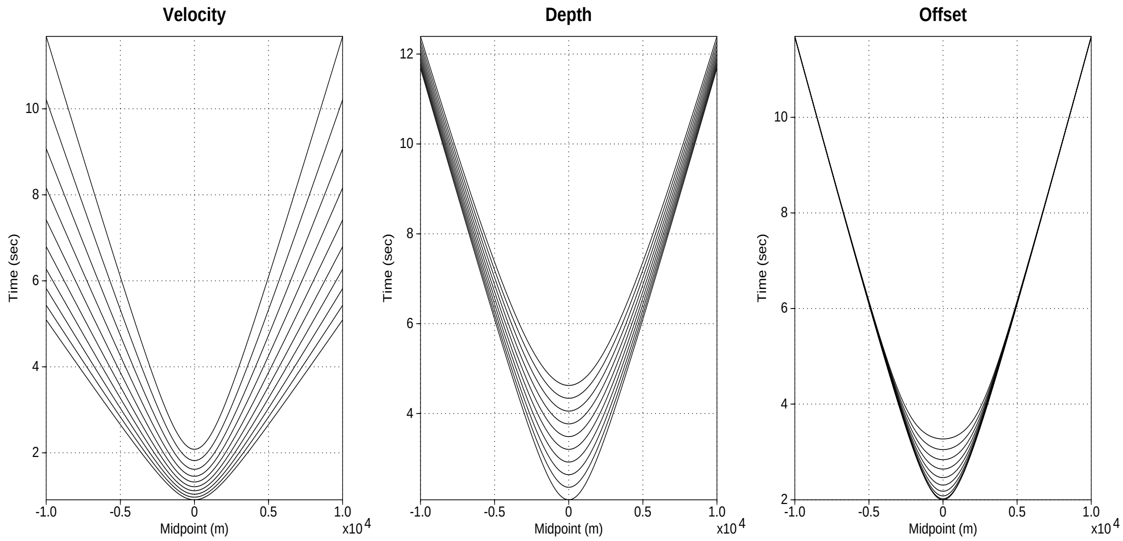

Figure 1: Cheops pyramid changes with different parameters. (**L**) From top to bottom, the hyperbolic moveout curves become flatter when velocity increases. (**M**) From bottom to top, the curves become flatter with the increase of depth. (**R**) From bottom to top, the hyperbolic curves change from zero to nonzero offset. yalei1-cheops [NR]

weighting function depends only on imaging depth and offset. As shown in Figure 3, the weighting function has a double-peaked shape in non-zero offset. This feature is very interesting. Intuitively, it is very natural to think that the data value located right in the middle of the panel should have the largest contribution to the image. The double-peaked weighing function in the case of common-offset configuration suggests that the largest contribution to the image is not from the middle of the integral curve, but from the two flanks. Therefore, it is very important to include the two peaks to get a true-amplitude image when choosing the integral aperture.

SYNTHETIC DATASET

Figure 4 shows a simple 2-D acoustic model based on one used by Dong and Keys (1997), as shown in Figure 4. The only difference is that all the layers here have a 10 degree dipping angle. For the first interface, there is no velocity change and only density change. According to equation (9), the reflection coefficient is constant, 0.05. Similarly, we can reach the same result from the acoustic AVO approximation. The second layer has changes in velocity and density, but in opposite signs. Therefore, these two changes cancel each other out and give a zero-valued intercept. Slope B

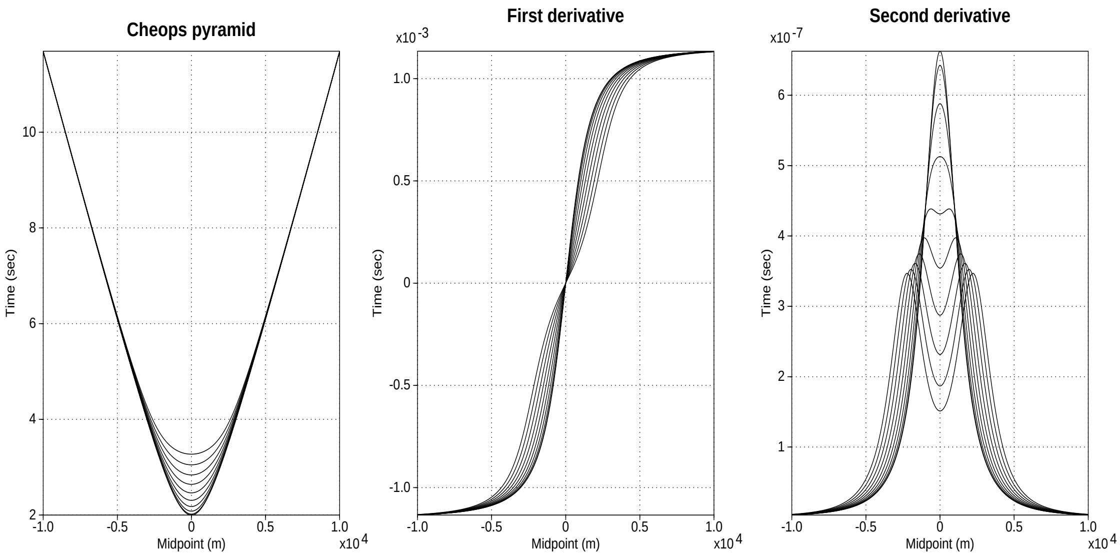

Figure 2: Cheops pyramid, first, and second derivatives. (**L**) Cheops pyramid changes from zero to nonzero offset. (**M**) The first derivative has two inflections points near the middle of the panel in the case of non-zero offset. (**R**) The second derivative has a corresponding double-peaked shape in non-zero offset. yalei1-deri [NR]

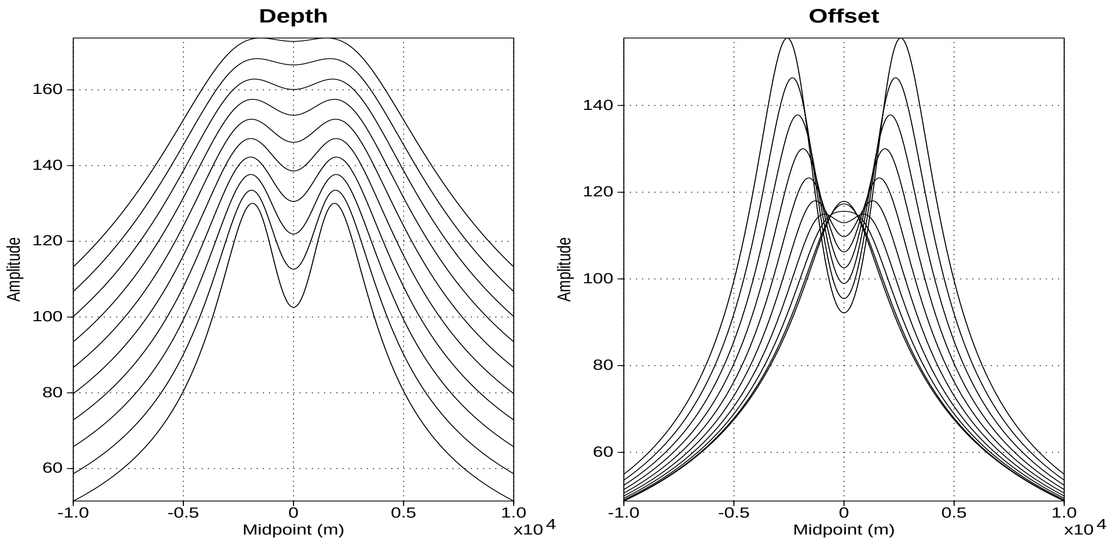

Figure 3: The weighting function changes with depth and offset. (**L**) With increasing depth, the double peaks smear out. (**R**) From zero to nonzero offset, the weighting function goes from single-peaked to double-peaked shape. yalei1-weight [NR]

is equal to 0.05. Reflection coefficient R increases from zero to nonzero value with the increase of the incident angle. The third interface has only a velocity change and no density change. The velocity drops across the interface and results in a negative intercept and slope. We use an acoustic modeling program developed by Dong, which

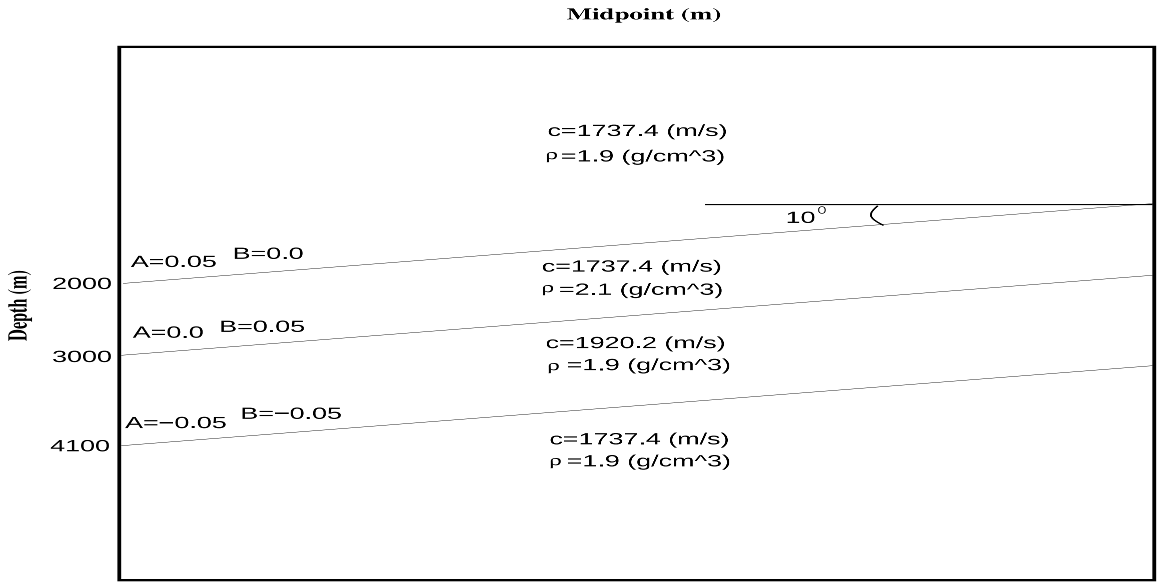

Figure 4: Dipping acoustic velocity model used in generating the synthetic dataset. yalei1-model [NR]

is based on the reflectivity method (Müller, 1985). For such kind of layer model, the modeling result is not only kinematically, but also dynamically exact. As shown in the following result, such an accurate modeling program is very helpful for verifying the performance of our inversion program. Figure 5 is a common-shot gather. The first two events have a similar pattern, except that the second one goes to a zero-valued amplitude in the near offset. However, the third event shows an opposite pattern. Figure 6 shows an image gather from the inversion result. Since the correct velocity model has been used in calculating the WKBJ Green's function, the three events have been flattened in the image gather. However, due to the NMO stretching effect, the events broaden from near to far offset. One way to check the accuracy of our inversion result is to pick the peak amplitude along the three events and then compare it with the theoretical solution. Figure 7 shows that the numerical results match the theoretical ones very accurately. Figure 8 and 9 shows the intercept A and slope B estimated from the inversion result. Compared with the theoretical results under acoustic approximation, our solution matches the theoretical one very well. These two figures also show the stretching effect very clearly. How to remove this stretch effect efficiently is our next research topic.

Figure 5: Common-shot gather generated from the dipping velocity model using the reflectivity method. yalei1-shot [NR]

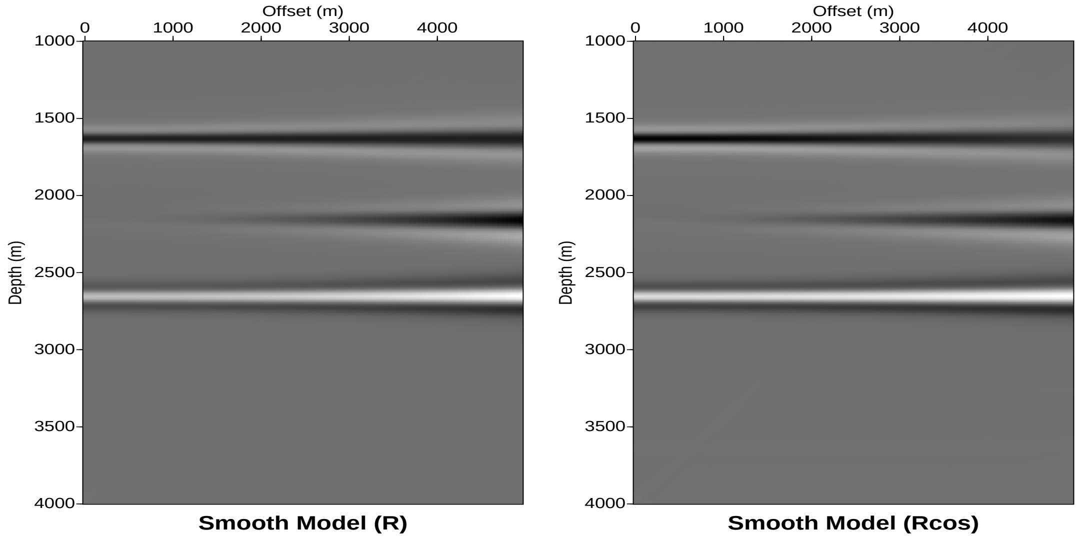

Figure 6: Common-image gather of the inversion result. (**L**) R as a function of offset. (**R**) $R\cos\theta$ as a function of offset. yalei1-dip-cig [NR]

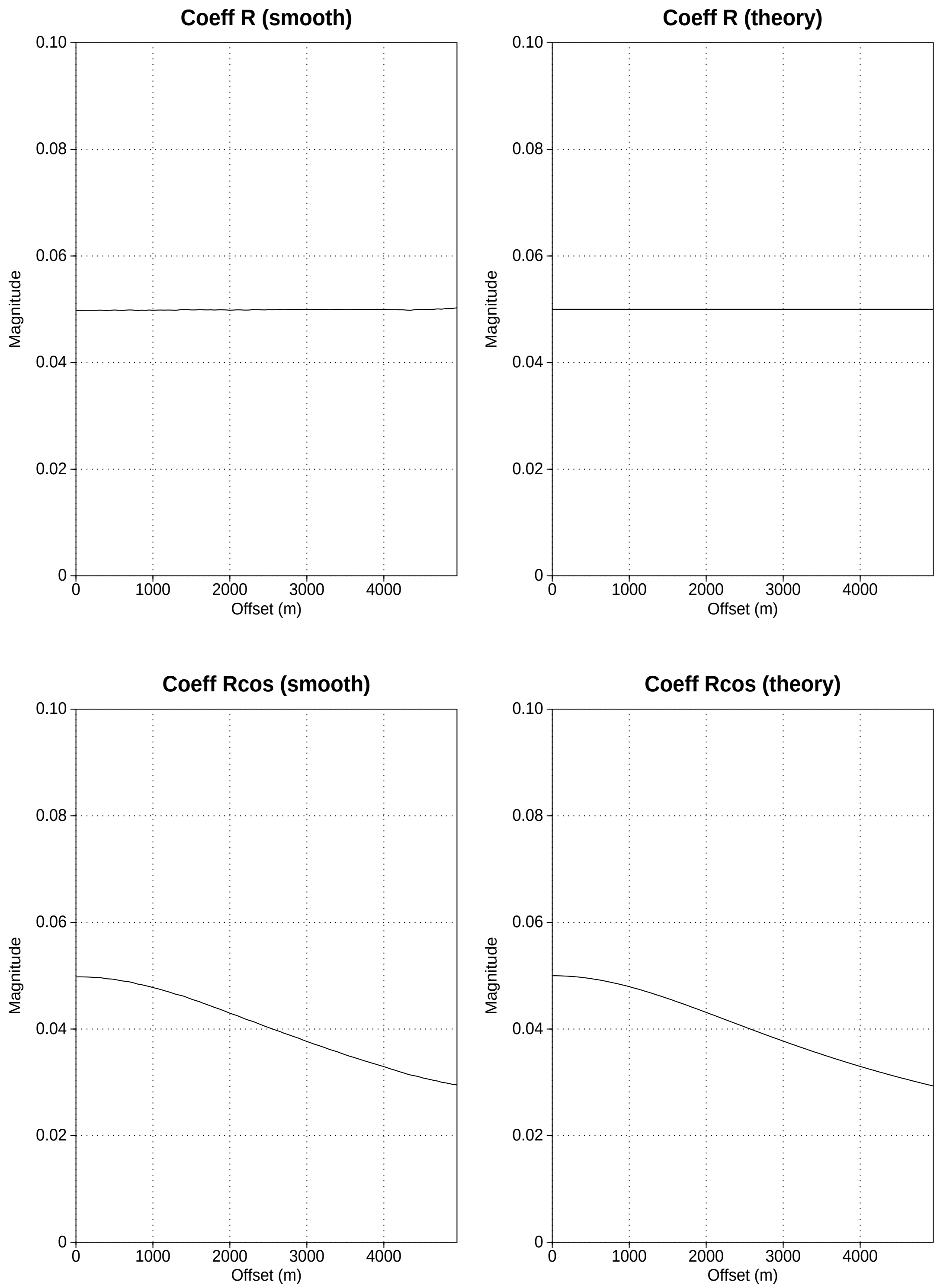

Figure 7: Comparison of numerical result and theoretical result. (**TL**) Numerical R. (**TR**) Theoretical R. (**BL**) Numerical $R\cos\theta$. (**BR**) Theoretical $R\cos\theta$. yalei1-compare [NR]

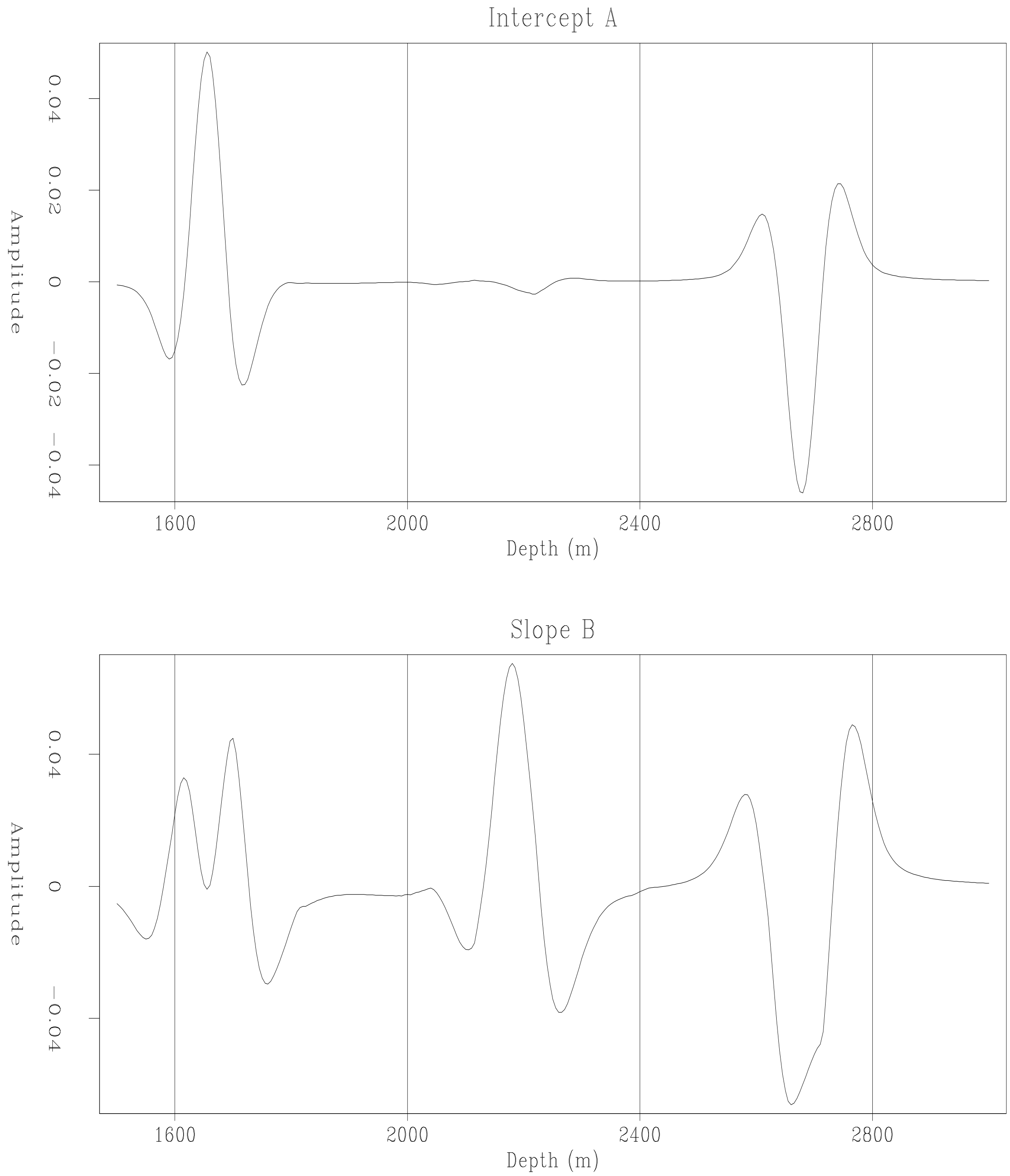

Figure 8: AVO coefficients A and B. (**Top**) Intercept A. (**Bottom**) Slope B. The stretch effect is very obvious in the first wavelet of slope B. Since the transmission effect has not been taken into account, the absolute values for the second and third events are less accurate. yalei1-dip-avo [NR]

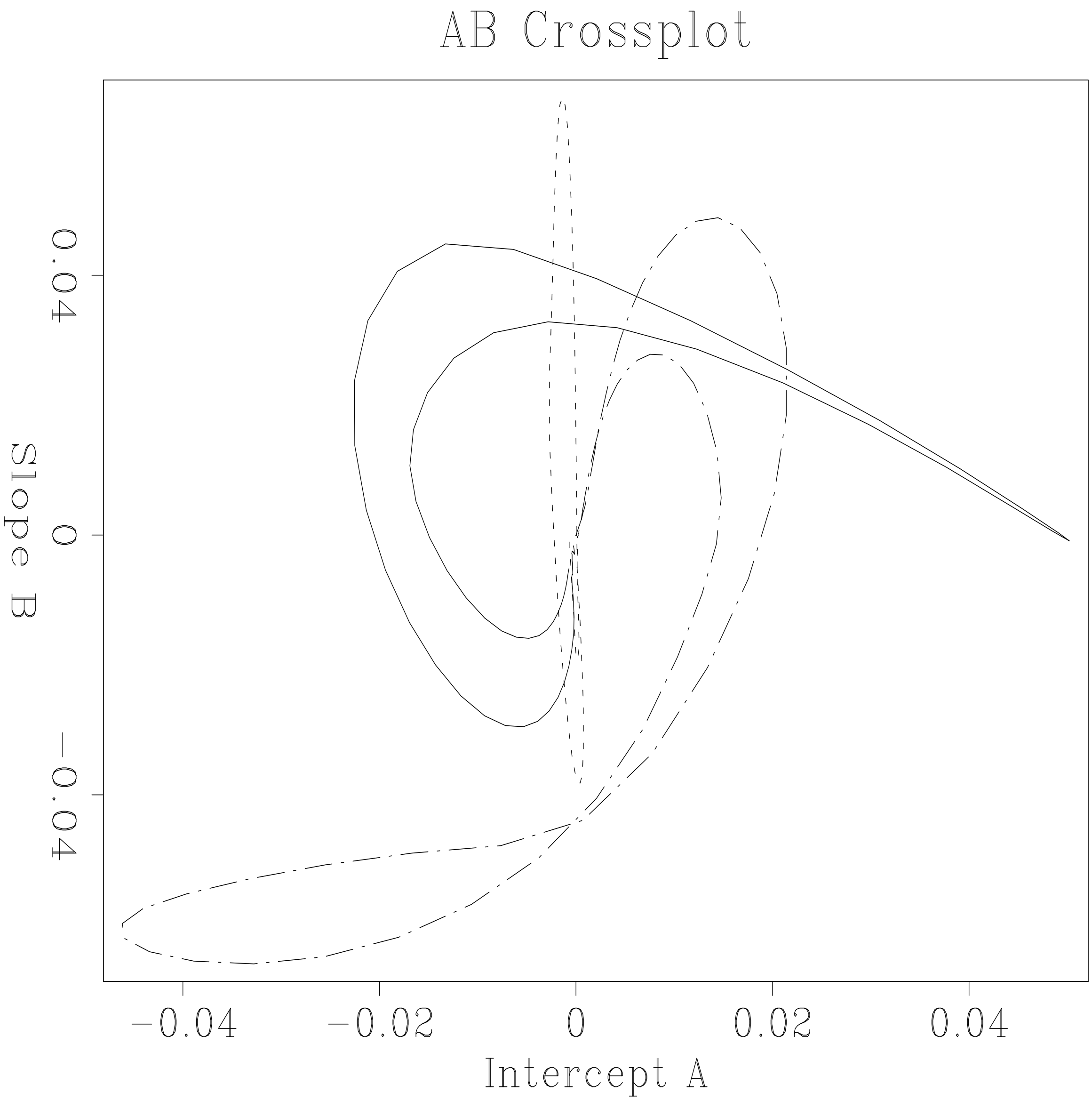

Figure 9: Crossplot of intercept A and slope B. The solid curve represents the first event, the dashed-line curve corresponds to the second one, and the dashed-dotted curve is linked with the third event. The swirly nature of the curves is due to NMO stretch (Dong, 1996). The extent of stretching effect can be evaluated by the distance between the curves and the original point. yalei1-crossplot [NR]

THE MOBIL AVO DATA AND ITS RESULT

The Mobil AVO dataset is a marine dataset collected from the North Sea. The dataset contains strong water-bottom multiples. Before AVO analysis, some processing procedures have been applied to the data to remove the multiple energy. All together, there are 952 CMP gathers with 25m sampling intervals. Each gather contains 60 traces, the offset sampling interval is 50m and the near offset is 288m. The trace length is 1000 samples (sampling rate = 4ms). There are two well logs available at CMP-809 and CMP-1571. In well CMP-809, the density, V_p, and V_s were recorded from 1km to 3.15km. On the basis of this well's information, Dong and Keys (1997) built up a 12-layer (some with vertical gradient) background velocity model for the inversion. Since our new approach can output common-image gathers (CIG), we initially use this model in our inversion and then check the accuracy of this layered model. As shown in 10, the events from the old velocity model bend upwards, which means the interval velocity in the old model is lower than the correct one. We then conducted a conventional velocity analysis. After converting the RMS velocity model into an interval velocity model, we applied the new velocity model to the dataset and produced the new common-image gather at the same CMP location. It is clear that the new velocity model is better for imaging and inversion (Figure 10). By stacking the common-offset inversion result, we got a R and R' section (Figure 11). After obtaining the Kirchhoff inversion result, we estimated the cosine of the specular angle θ. According to the elastic AVO approximation theory, we estimated of intercept A and slope B, as shown in Figure 12. Furthermore, we combined the intercept and slope sections and produced a fluid-line section, which shows the V_p/V_s anomaly (Figure 13).

CONCLUSION AND DISCUSSION

We implemented an AVO inversion algorithm in $V(x,z)$ media. Our approach is a two-step inversion scheme:

- 2.5-D Kirchhoff inversion;
- AVO coefficient estimation.

Since the velocity model used in AVO analysis is relatively smooth, the finite-difference forward modeling result is accurate enough in Kirchhoff inversion. Both the synthetic and field data example can verify the accuracy of the finite-difference scheme. On the basis of Bleistein et al. (1987), we proposed another pair of Kirchhoff inversion operators that have a more obvious physical meaning. One is the specular reflection coefficient R, and the other is R multiplied by the cosine of half of the specular incident angle, $R' = R\cos\theta$. The reflection coefficient R, organized into common-image gathers, is not only necessary in estimating the AVO intercept A and slope B, but also

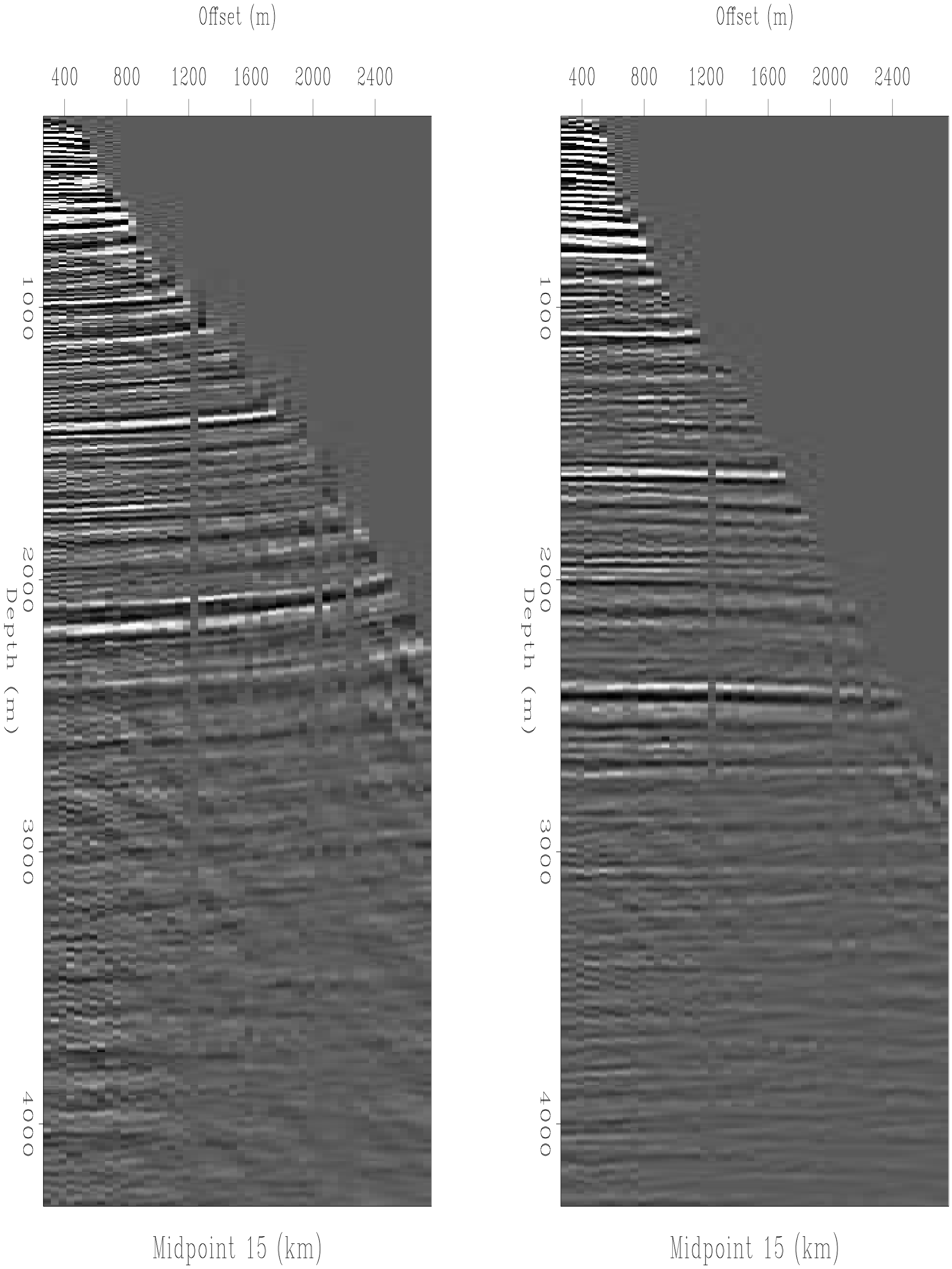

Figure 10: Common-image gathers of the Mobil AVO dataset. (**L**) CIG from the old velocity model. (**R**) CIG from the new velocity model. Both are from the same midpoint location. The new model is significantly better than the old one. In the old CIG, because of the use of a low velocity model, not only can the image event not be flattened, it also has a depth shift from top to bottom. yalei1-mobil-cig [NR]

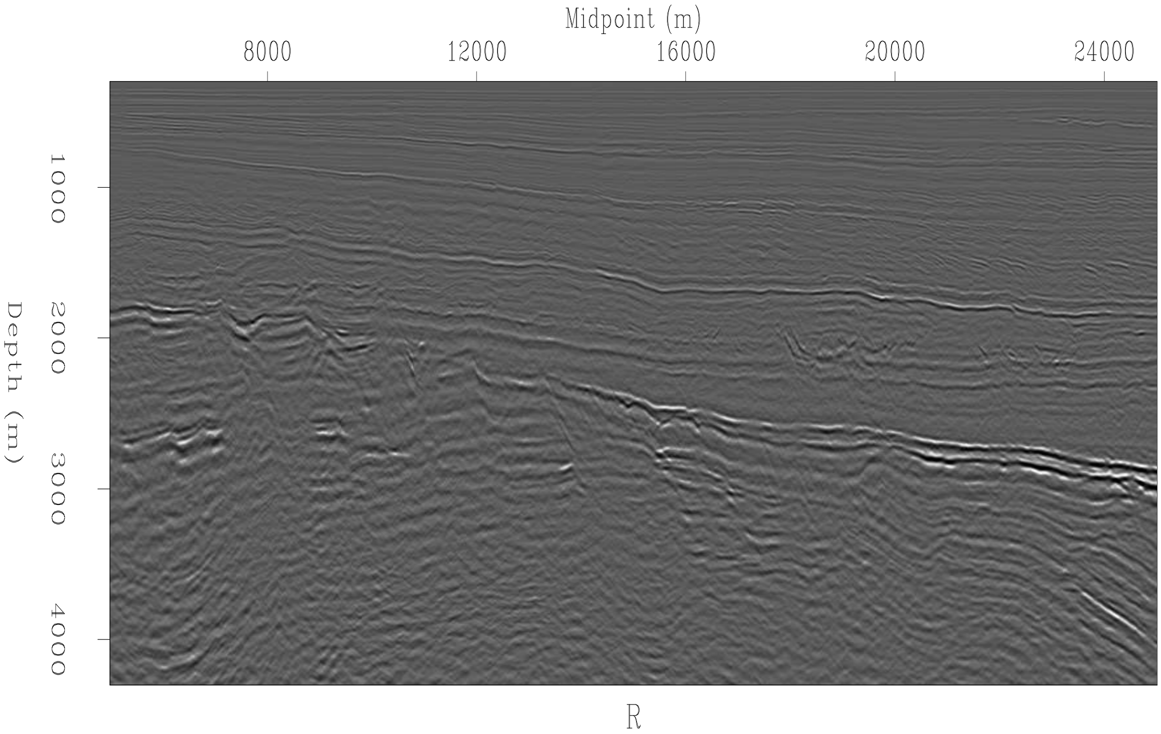

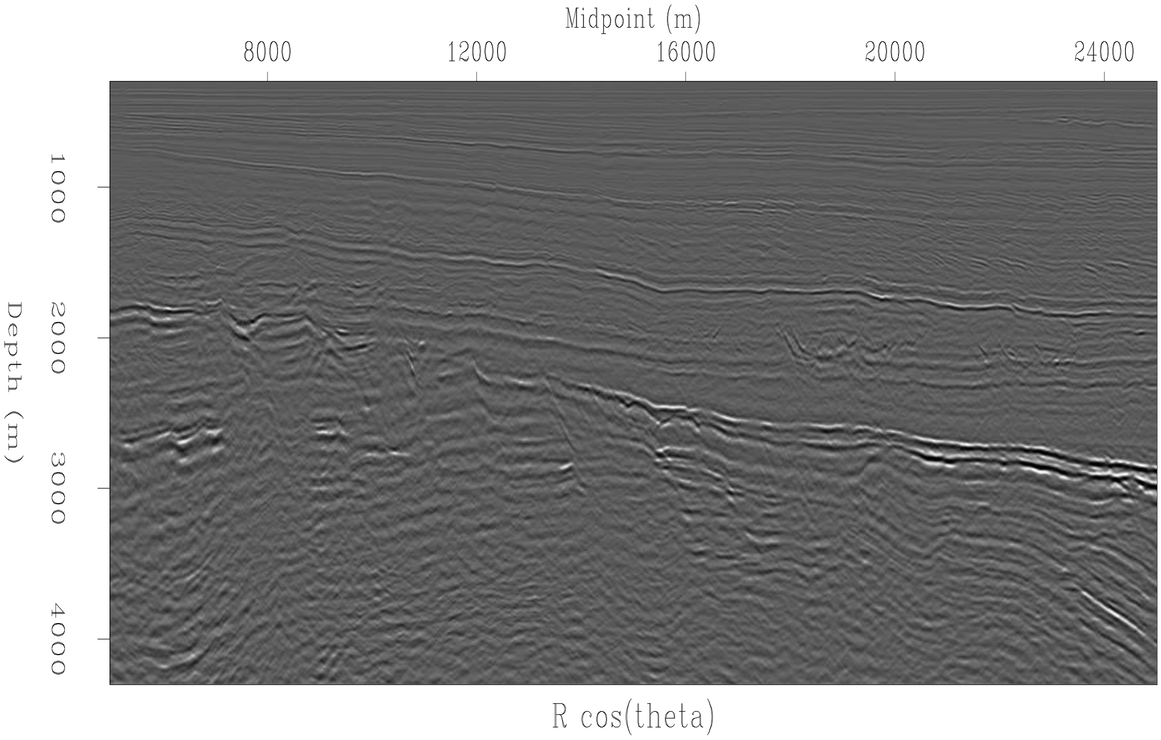

Figure 11: The stacked section of the inversion result. (**Top**) Reflection coefficient R. (**Bottom**) $R\cos\theta$. The diffraction energy has been well collapsed. yalei1-mobil-stack [NR]

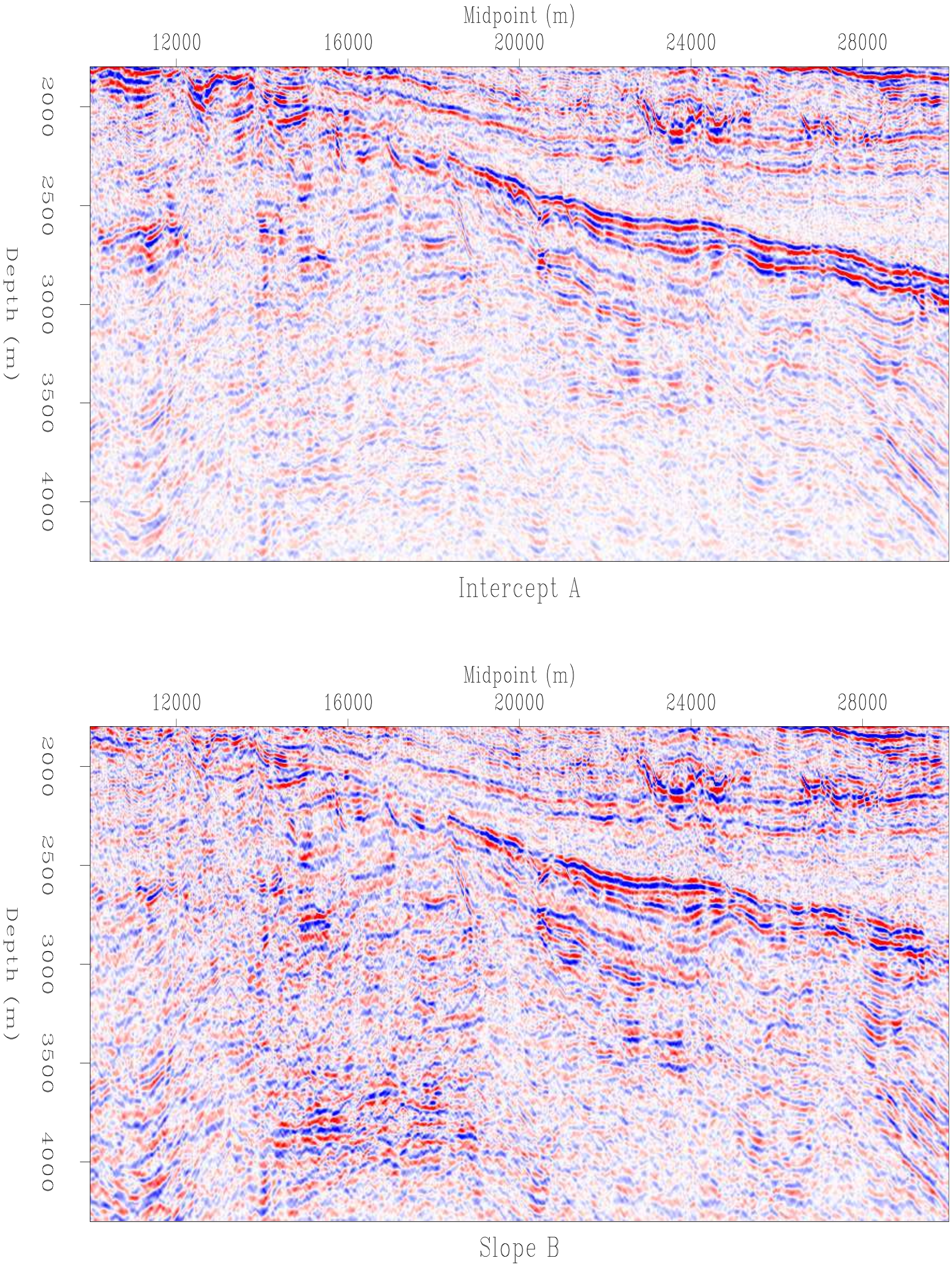

Figure 12: AVO coefficient sections of the Mobil AVO dataset. (**Top**) Intercept A section. (**Bottom**) Slope B section. Similar to the stacked section, the diffraction energy has also been well collapsed in the A and B section. Generally, intercept A and slope B have opposite polarities. Slope B has a larger value than intercept A. yalei1-mobil-avo [NR]

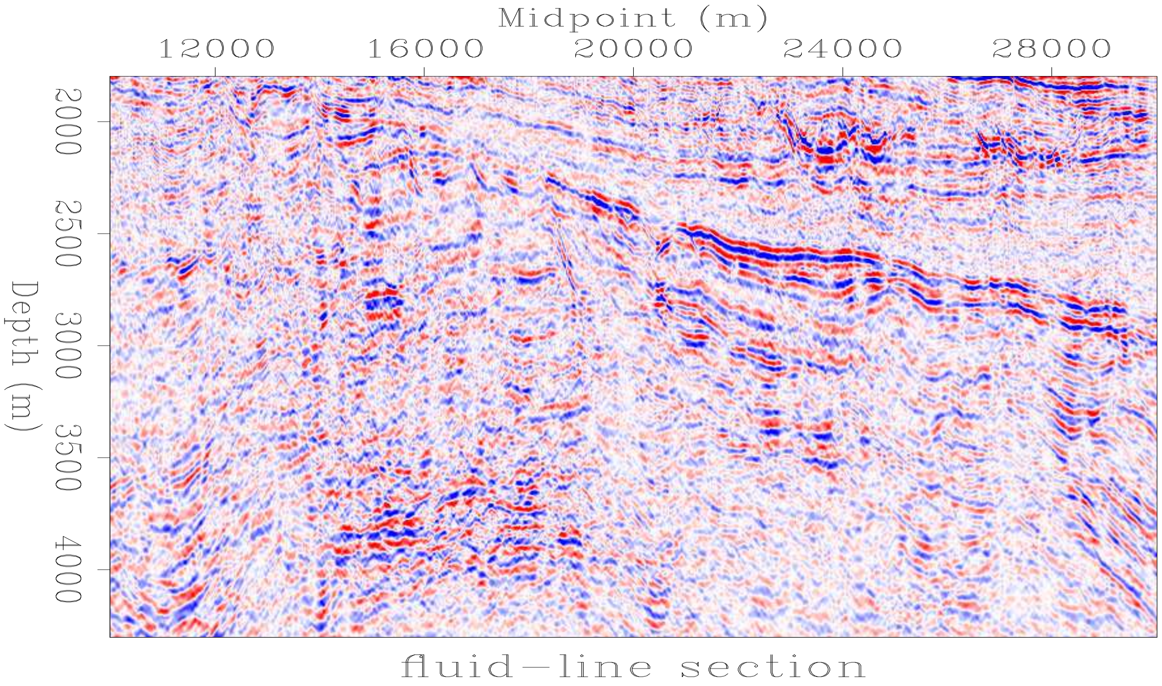

Figure 13: The fluid-line section of the Mobil AVO dataset. Many strong events in A & B section have been canceled. The strong event in the middle of the section shows the anomaly of V_p/V_s, which may be an indicator of hydrocarbon in that area. yalei1-fluid-line [NR]

essential to update the velocity model. Through checking common-image gathers, we can update the velocity model and produce a more accurate image. This feature will also prevent the velocity error from propagating into the final AVO coefficients. One of the fundamental differences between Kirchhoff inversion and Kirchhoff depth migration is that Kirchhoff inversion has an extra weighting function varying along the integral curves. We investigated the relationship between the weighting function and double-square-root (DSR) equation in the homogeneous medium. It is interesting to see that the weighting function has double peaks in the common-offset configuration. This observation tells us that the largest contribution to the image is not from the middle of the integral curve, but from the two flanks. Therefore, it is very important to include the locations of the two peaks in order to recover a true-amplitude image. We applied our algorithm to both synthetic and field datasets. The synthetic example shows that this new scheme is very accurate in calculating the reflection coefficient and the specular incident angle. When applying our approach to the Mobil AVO dataset, we updated the velocity model according to the common-image gathers. Furthermore, we estimated the AVO coefficients, intercept A and slope B, and then created a fluid-line expression of V_p/V_s anomaly. Our result shows that there is a strong V_p/V_s anomaly in the middle section that suggests a potential hydrocarbon indicator.

REFERENCES

Aki, K., and Richards, P. G., 1980, Quantitative seismology: Theory and methods: W. H. Freeman and Co., New York.

Beylkin, G., 1985, Imaging of discontinuities in the inverse scattering problem by inversion of a casual generalized Radon transform: J. Math. Phys., **26**, 99–108.

Bleistein, N., Cohen, J. K., and Hagin, F. G., 1987, Two and one-half dimensional Born inversion with an arbitrary reference: Geophysics, **52**, no. 1, 26–36.

Claerbout, J. F., 1985, Imaging the Earth's Interior: Blackwell Scientific Publications.

Dong, W., and Keys, R. G., 1997, Multi-parameter seismic inversion for hydracarbon detection: 15th World Petroleum Congress Proceedings.

Dong, W., 1996, Fluid-line distortion due to migration stretch: 66th Ann. Internat. Mtg., Soc. Expl. Geophys., Expanded Abstracts, 1345–1348.

Lumley, D. E., Nichols, D., Ecker, C., Rekdal, T., and Berlioux, A., 1995, Amplitude-preserved processing and analysis of the Mobil AVO data set: SEP–**84**, 125–152.

Mosher, C. C., Keho, T. H., Weglein, A. B., and Foster, D. J., 1996, The impact of migration on AVO: Geophysics, **61**, no. 6, 1603–1615.

Müller, G., 1985, The reflectivity method: a tutorial: J. Geophys., **58**, 153–174.